Journal of Alloys and Compounds 585 (2014) 713–721

Contents lists available at ScienceDirect

Journal of Alloys and Compounds

journal homepage: www.elsevier.com/locate/jalcom

Selective laser melting additive manufacturing of Inconel 718 superalloy parts: Densification, microstructure and properties

Qingbo Jia, Dongdong Gu *

College of Materials Science and Technology, Nanjing University of Aeronautics and Astronautics (NUAA), Yudao Street 29, 210016 Nanjing, PR China

ARTICLE INFO

Article history:
Received 6 August 2013
Received in revised form 12 September 2013
Accepted 16 September 2013
Available online 10 October 2013

Keywords:
High-temperature alloys
Laser processing
Microstructure
Selective laser melting (SLM)

ABSTRACT

This paper presented a comprehensive study of densification behavior, microstructural features, microhardness, wear performance and high-temperature oxidation properties of Inconel 718 parts fabricated by selective laser melting (SLM), a typical additive manufacturing process. The relationship of processing conditions, microstructures and material properties was established. The occurrence of balling phenomenon at a lower laser energy density input reduced the relative density of the formed parts. A reasonable increase in laser energy density yielded a near-full densification. The typical microstructures of SLM-processed Inconel 718 parts experienced successive morphological changes on increasing the applied laser energy density: coarsened columnar dendrites – clustered dendrites – slender and uniformly distributed columnar dendrites. The optimally prepared fully dense Inconel 718 parts had a uniform microhardness distribution with a mean value of 395.8 $HV_{0.2}$, a considerably low friction coefficient of 0.36 and a reduced wear rate of 4.64×10^{-4} $mm^3/N\,m$ in sliding wear tests. The formation of an adherent tribolayer on the worn surface contributed to the improvement of wear performance. The high-temperature oxidation resistance was enhanced as the applied laser energy density increased and the elevated high-temperature oxidation property was primarily attributed to the formation of refined microstructural architectures of SLM-processed parts.

1. Introduction

Nickel-based superalloys have experienced extensive development and found enormous attractions over the past four decades [1,2]. Inconel 718, a Ni–Cr–Fe austenite (γ) superalloy, has been widely employed in many applications such as turbine blades, combustion chambers and nuclear reactors owing to its excellent creep properties, oxidation resistance and hot corrosion resistance [3–5]. Typically, Inconel 718 superalloy has been developed and applied in wrought, cast, and powder metallurgy (normally with HIP treatment) forms and the as-produced Inconel 718 parts using these conventional methods have demonstrated the reasonable microstructural and mechanical properties [6–8]. As a core element of the hot-end structural components, Inconel 718 can retain its superior mechanical properties in a broad range of temperatures by virtue of solid–solution strengthening and precipitation strengthening. Nevertheless, its high hardness and low thermal conductivity characteristics make it difficult to apply conventional machining methods because of tool over-wear and poor workpiece surface integrity [9]. With the rapid development of modern industry, Inconel 718 parts with complex structures, high dimension precision and further elevated mechanical properties are on higher demand [10,11]. Therefore, the application of the novel non-traditional processing technology is necessary to the net-shape production of Inconel 718 parts with complex configurations and high performance.

Selective laser melting (SLM), which is based on the principle of material incremental manufacturing, has been recognized as a promising additive manufacturing (AM) technology, due to its flexibility in feedstock and shapes [12–15]. In the case of SLM, it creates the three-dimensional dense parts directly from the user-defined CAD data, using a computer controlled scanning laser beam as the energy source to melt the pre-spread powders selectively in a layer-by-layer manner [16–18]. Furthermore, the geometrically complex components with high dimensional precision and good surface integrity can be obtained precisely by the SLM process without subsequent process requirements, which the conventional methods cannot keep pace with easily [19]. However, the desired microstructures of SLM-processed parts are inevitably affected by complicated physical and chemical behaviors within the molten pool, as a result of the non-equilibrium processing technique of laser. Significant research efforts are still required to focus on microstructures and properties of the fabricated parts under various processing conditions.

* Corresponding author. Tel./fax: +86 25 52112626.
E-mail address: dongdonggu@nuaa.edu.cn (D. Gu).

0925-8388/$ - see front matter © 2013 Elsevier B.V. All rights reserved.
http://dx.doi.org/10.1016/j.jallcom.2013.09.171

Many experimental investigations regarding microstructures and mechanical properties of laser processed Inconel 718 components have been carried out [20–22]. However, few studies on the effects of laser processing parameters on microstructure characteristics and mechanical behaviors have been published. Among previous mechanical performance studies, the vacancy of a systematic research on wear resistance of laser processed Inconel 718 parts needs to be made up urgently, considering its severe working conditions. Moreover, to the best of authors' knowledge, no previous work has been reported on high-temperature oxidation behaviors of Inconel 718 parts prepared by SLM process. In the present investigation, Inconel 718 samples were fabricated by SLM under various processing conditions. The effects of processing parameters on surface morphologies, phases and microstructures, and material properties were studied. The relationship between SLM process and microstructural and mechanical properties was established. Wear and high-temperature oxidation tests were implemented on SLM-processed Inconel 718 parts and the wear and oxidation processes were elucidated in detail. The underlying physical and chemical mechanisms for the development of microstructural and mechanical properties during SLM process are applicable and/or transferrable to other laser-based powder processing techniques, e.g. laser cladding, laser surface alloying, laser metal deposition (LMD), or Laser Engineered Net Shaping (LENS).

2. Experimental procedures

2.1. Powder material

The gas atomized Inconel 718 powders with the spherical shape and the particle size in a range of 15–45 μm were used as the starting materials in this study. The chemical compositions of Inconel 718 powders are given in Table 1.

2.2. Laser processing

The SLM experimental setup consisted of an IPG Photonics Yitterbium YLR-200-SM fiber laser with a power of ~200 W and a spot size of 70 μm, an automatic powder layering apparatus, an inert argon gas protection system and a computer system for process control. Based on a series of preliminary experiments, the laser power (P) was preset at 110, 110, 120, 130 W and scan speeds (v) were set at 600, 400, 400, 400 mm/s, respectively. Thus, four different linear laser energy densities η of 180, 275, 300 and 330 J/m, which were defined by [23]:

$$\eta = P/v \tag{1}$$

were used to appraise the influence of the energy input per unit length with respect to the layer results. Cubic specimens with dimensions of 8 mm × 8 mm × 6 mm were prepared using SLM (Fig. 1).

2.3. Microstructural characterization

Phase identification was performed by a D8 Advance X-ray diffractometer (XRD) with Cu Kα radiation at 40 kV and 40 mA, using a continuous scan mode. A quick scan at 4°/min was first performed over a wide range of 2θ = 30–100°. A slower scan rate of 1°/min was further applied over 2θ = 42–45° to give a more accurate determination of diffraction peaks. The fabricated samples were cut, inlaid and polished for metallographic observation in line with the standard procedures. The densification behaviors were revealed by using optical microscopy (OM). Microstructures were characterized using a Hitachi S-4800 scanning electron microscopy (SEM) with the samples being etched by a solution containing of HCl (10 ml) and H_2O_2 (3 ml) for 10 s. EDAX energy dispersive X-ray spectroscope (EDX) was utilized to determine the chemical compositions.

Table 1
Chemical compositions of Inconel 718 powder (in weight percent, wt%).

Cr	Mo	Al	Ti	Fe	Nb	C	Ni
18.4	4.2	0.3	0.9	17.7	5.1	0.08	Balance

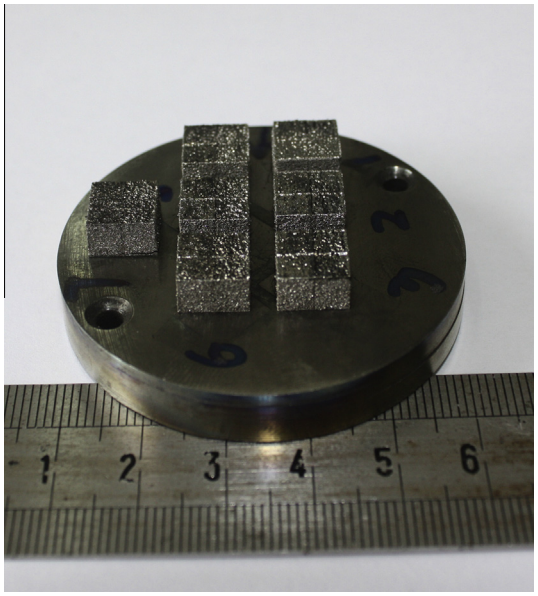

Fig. 1. Photograph of SLM-processed Inconel 718 parts.

2.4. Characterization of mechanical properties

The relative density of fabricated samples was determined based on the Archimedes principle. The Vickers hardness tests were carried out using a HXS-1000A microhardness tester at a load of 100 g and an indentation time of 10 s. Dry sliding wear tests were conducted in a HT-500 ball-on-disk tribometer at room temperature. A 3 mm diameter bearing steel GCr15 ball was taken as the counterface material, using a test load of 3 N. The friction unit was rotated at 560 rpm for 15 min and the rotation radius was 2 mm. The coefficient of friction (COF) was recorded during sliding. The wear volume (V) was determined gravimetrically using:

$$V = \frac{M_{loss}}{\rho} \tag{2}$$

where M_{loss} was the weight loss of the specimens after wear tests and ρ the density of SLM-processed parts. The wear rate (ω) was calculated by:

$$\omega = \frac{V}{WL} \tag{3}$$

where W was the contact load and L was the sliding distance.

2.5. High-temperature oxidation behavior

Samples in a rectangular contour were polished for high-temperature oxidation behavior investigations. The samples were rinsed with ethanol ultrasonically and then dried in a desiccator afterwards. Prior to oxidation, the specimens were weighed and the alumina crucibles heated repeatedly until no mass variations. The laboratory muffle furnace was preheated up to the testing temperature at 1123 K at atmospheric pressure in still air. Specimens with crucibles were subsequently exposed to the high-temperature and precisely weighted at each predetermined time. The weight gains were measured by the following equation:

$$\Delta W/S = (W_t - W_0)/S_0 \tag{4}$$

where $\Delta W/S$ represents the weight gain per unit surface area (mg/cm^2), W_t the weight before oxidation, W_0 the weight after oxidation, and S_0 stands for the surface area before oxidation.

3. Results and discussion

3.1. Phases

Typical XRD patterns of SLM-processed Inconel 718 parts are depicted in Fig. 2. In general, the strong diffraction peaks corresponding to γ′ Ni_3 (Al, Ti) with a $L1_2$ ordered face-centered cubic (fcc) crystal structure and γ (Ni–Cr–Fe) in a face-centered cubic (fcc) crystal structure were detected, which was in good agreement with some previous investigations on the constitutional phases of

laser processed Inconel 718 [8,24]. The 2θ locations of γ' precipitate were found to coincide with the γ matrix within a large range of 2θ degrees (Fig. 2a). Further XRD characterization within small $2\theta = 42–45°$, as shown in Fig. 2b, were carried out in order to distinguish the existent phases accurately. The 2θ location as well as the intensity of the detected γ and γ' peaks are listed in Table 2, respectively. According to Fig. 2b and Table 2, the diffraction peaks of γ and γ' became considerably broadened and the intensity showed a significant decrease, implying the formation of small-sized crystalline grains of SLM-processed parts with the enhancement of η. Moreover, as the applied η increased above 300 J/m, the 2θ locations of the diffraction peaks shifted to higher 2θ. In the principle of Bragg's law [25]:

$$2d\sin\theta = n\lambda \quad (n = 1, 2, 3, \cdots) \tag{5}$$

the observed increase of 2θ indicated a decrease in the distance between adjacent lattice planes (d), which is believed to be caused by the distortion of lattice due to the incorporation throughout the γ matrix.

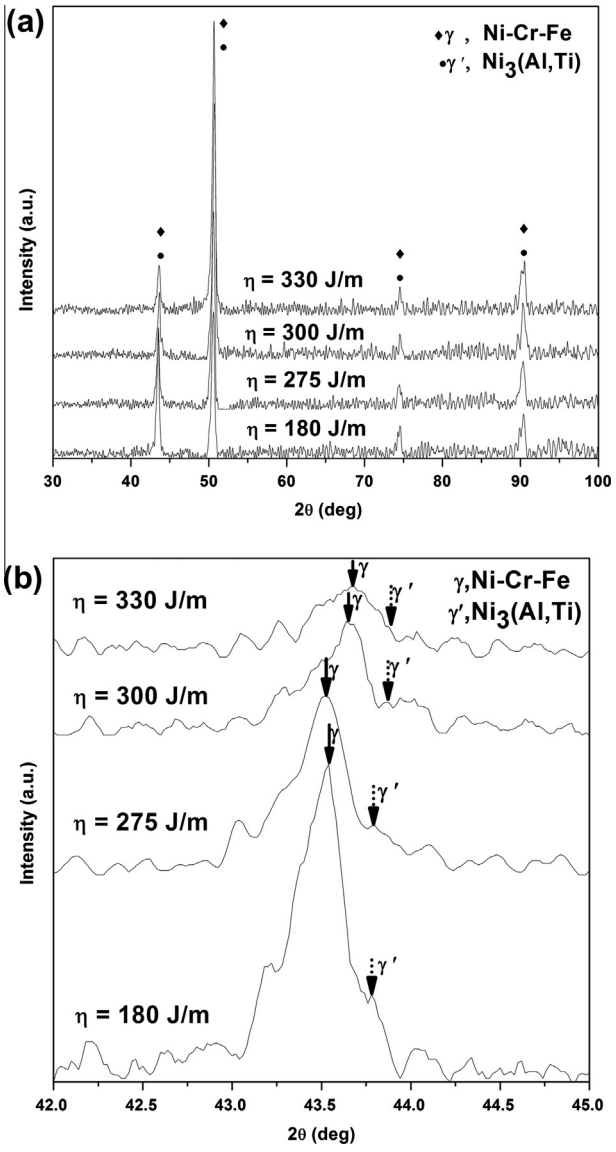

Fig. 2. XRD spectra of SLM-processed Inconel 718 parts at different processing conditions obtained in a wide range of $2\theta = 30–100°$ (a) and obtained in a small range of $2\theta = 42–45°$ (b).

3.2. Surface morphologies and densification

The SEM images in Fig. 3 show the typical surface morphologies of Inconel 718 parts processed using various parameters. The surface integrity varied significantly for the different linear laser energy densities (η). The changes in measured relative densities and the cross-section morphologies of corresponding parts are illustrated in Fig. 4. At a lower η of 180 J/m, the scanning tracks were observed to be discontinuous, having large-sized balls surrounded by open-pores presented on laser processed surface (Fig. 3a). In this instance, the formation of irregular and accumulated pores on cross-section restricted the densification response by merely 73.6% (Fig. 4). On increasing applied η by reducing scan speed, the scanning tracks became uninterrupted even though rudimentary balls with residual shrinkage cavities were still present (Fig. 3b). The pores on cross-section were dispersed and diminished, which increased the densification level to 86.8% (Fig. 4). The balling phenomenon was alleviated and the resultant densification rate increased at an even higher η of 300 J/m, resulting in a relatively smooth surface with few remnant scattered metallic globules (Fig. 3c). As η of 330 J/m was properly settled, sound surface morphology free of any pores or balls was obtained (Fig. 3d), achieving a dense cross-section in near-full 98.4% density (Fig. 4).

In the present investigation, the smooth and dense surface was obtained by the coordination between laser power and scan speed during the shaping process. At a relatively high scan speed and the resultant low η, the dwelling time of the laser beam on the surface of molten pool became shortened, thereby weakening the operative temperature of the pool. The dynamic viscosity μ of a SLM system with an entirely liquid formation is temperature-dependent [26]. The higher dynamic viscosity of Inconel 718 liquid was obtained as a consequence of the lower temperature within the molten pool. The influence of high viscosity at a high scan speed impeded the Inconel 718 liquid from spreading out smoothly, which in turn caused the formation of open-pores (Fig. 3a) and limited relative density (Fig. 4). Likewise, the balling effect connected with SLM process was also responsible for the undesirable surface finishes and densification response. According to previous studies [27,28], the instability of liquid track can be inhibited based on the premise of $\lambda < \pi D$, where λ is the laser wavelength and D is the initial diameter of an unperturbed liquid cylinder. Higher scan speed accompanied with lower energy input resulted in a rapid decrease of diameter D of the cylinder at a constant laser wavelength λ. As a result, the instability of the liquid cylinder enhanced and generally tended to alter its shape so as to reduce the surface energy. This caused the breaking up of the liquid cylinder into a final equilibrium spherical form, whereas discontinuous scanning tracks occurred subsequently (Fig. 3a). Thus it was pertinent to conclude that balling effect was a severe barrier to the surface integrity and densification of SLM-processed Inconel 718 parts [29]. With the increment of η, the densification rate increased progressively, due to the weakened dynamic viscosity and balling phenomenon (Fig. 3b and c). Consequently, as η was properly settled, the entirely dense part with smooth surface morphology (Fig. 3d) was obtained.

Table 2
XRD data showing the displacement of identified peaks for Inconel 718 parts.

Sample (J/m)	γ		γ′	
	2θ (°)	Intensity (CPS)	2θ (°)	Intensity (CPS)
180	43.54	355	43.78	189
275	43.54	286	43.78	177
300	43.64	256	43.88	171
330	43.68	212	43.9	148

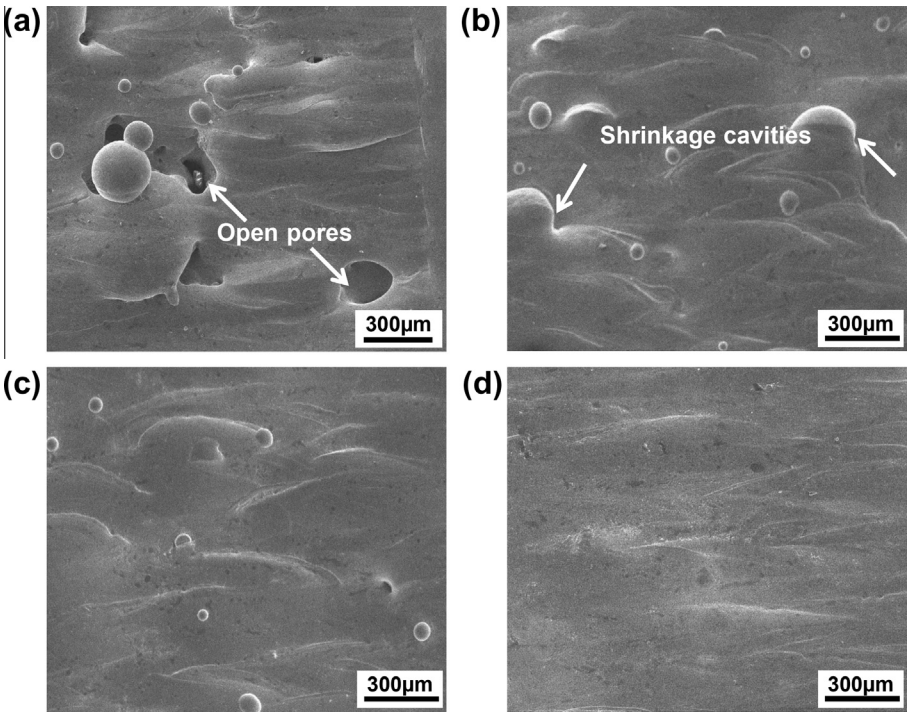

Fig. 3. SEM images showing typical surface morphologies of SLM-processed Inconel 718 parts at various laser energy densities, laser powers and scan speeds: (a) 180 J/m, 110 W, 600 mm/s; (b) 275 J/m, 110 W, 400 mm/s; (c) 300 J/m, 120 W, 400 mm/s; (d) 330 J/m, 130 W, 400 mm/s.

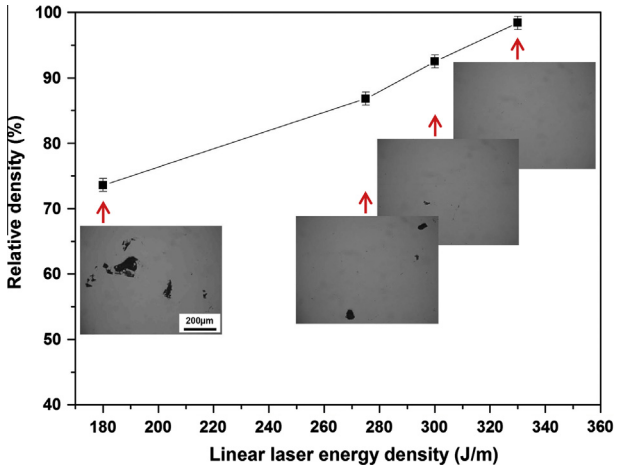

Fig. 4. Effect of laser energy density on densification rate of SLM-processed Inconel 718 parts. OM micrographs of cross-sections of the corresponding parts are included.

3.3. Microstructures and compositions

Fig. 5 shows the influence of linear laser energy density (η) on microstructures of SLM-processed Inconel 718 parts observed at a relatively low magnification. In order to study the characteristic microstructures clearly, higher magnifications on the specific positions in the structures were investigated (Fig. 6). Coarsened columnar dendrites in a fragmentized feature, which were identified as γ by XRD, were obtained at a lower η combined with higher scan speed (Fig. 5a). The columnar dendrites were found long-cracked in the center of the whole trunk and short-cracked in the interdendritic region at a magnified state (Fig. 6a). As the scan speed decreased, the dendrites arrays refined significantly (Fig. 5b), exhibiting a typical epitaxial growth along the building direction (indicated by the arrow). However, as shown in Fig. 6b, it was difficult to distinguish every dendrite due to its severe clustering occurred during the solidification process within the molten pool. The primary columnar dendrites became dispersed at an elevated laser power even though the columnar dendrites were irregularly arranged (Fig. 5c). Disconnected dendrite architectures with incomplete precipitants at inter-dendritic zone were observed at a higher magnification (Fig. 6c). When a further enhanced laser power was settled properly, the directional solidified slender columnar architectures were achieved eventually (Figs. 5d and 6d).

SLM of Inconel 718 parts were performed based on a complete melting and solidification manner and the columnar γ dendrite architecture was formed by means of the heterogeneous nucleation of γ nuclei and subsequent dendrite growth. According to the Gibbs–Thomson temperature equation, the dendrite tip temperature T_t is expressed as [30]:

$$T_t = T_M + eC_{Li}^* - \frac{RT_M^2}{\Delta H_f} \cdot \frac{V_t}{V_0} \tag{6}$$

where T_M is the melting point of the pure component, e the liquids slope, C_{Li}^* the liquid solute concentration at the solid–liquid interface, ΔH_f the latent heat of the material, V_t the growth rate of dendrite tip, and V_0 is the kinetic constant. V_t is controlled by laser beam scan speed v and can be determined by [31]:

$$V_t = v \cos \vartheta \tag{7}$$

where ϑ is the angle between the vectors V_t and v. Eq. (7) reveals that V_t is proportional to v and, thus, using a higher scan speed leads to a faster development rate of dendrites. Columnar dendrites could therefore be obtained at higher scan speed of 600 mm/s which showed an obviously coarsened morphology than that of 400 mm/s. Furthermore, residual thermal stress as a result of the repeated rapid melting and rapid solidification at a higher scan speed was remained in the workpiece [32], giving rise to the generation of thermal cracks in both dendrite and interdendritic zones (Fig. 6a).

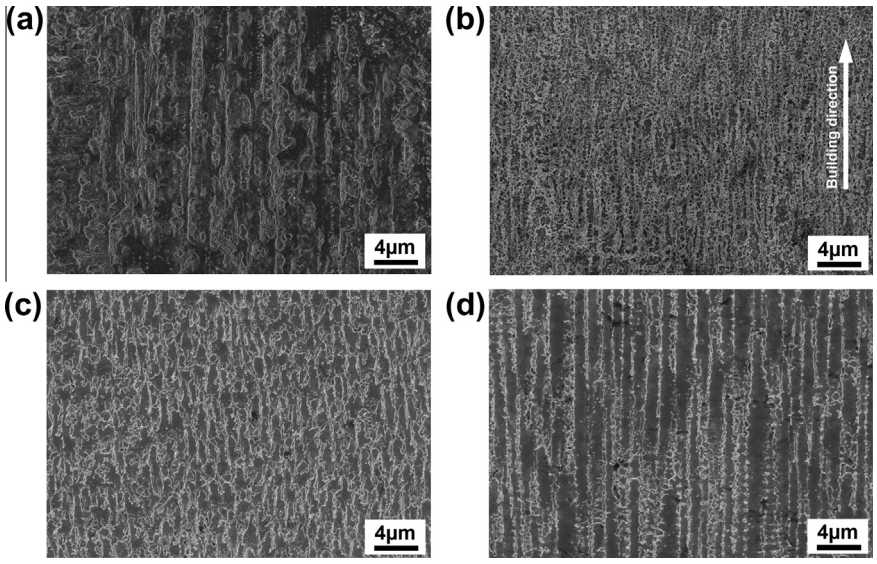

Fig. 5. SEM images showing characteristic microstructures of SLM-processed Inconel 718 parts at different laser energy densities, laser powers and scan speeds: (a) 180 J/m, 110 W, 600 mm/s; (b) 275 J/m, 110 W, 400 mm/s; (c) 300 J/m, 120 W, 400 mm/s; (d) 330 J/m, 130 W, 400 mm/s.

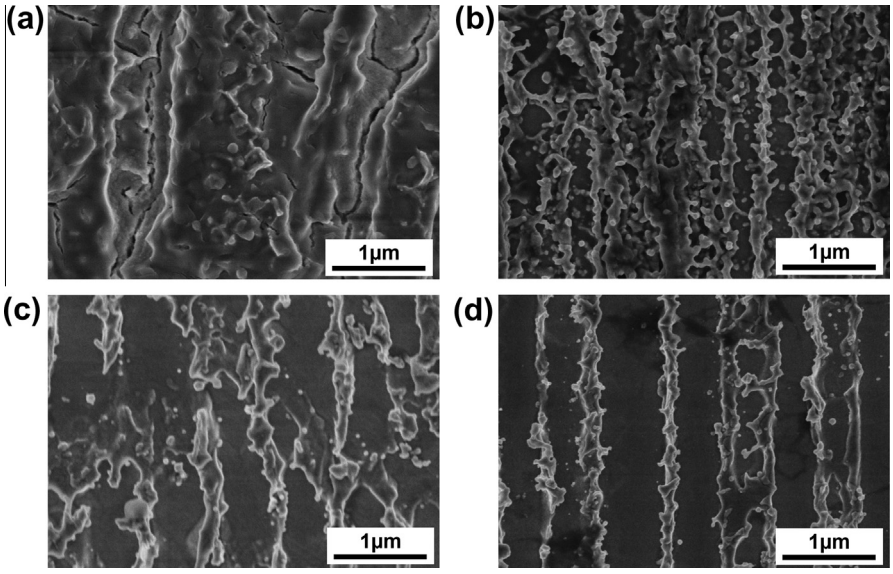

Fig. 6. High-magnification SEM images showing the characteristic microstructures of the crystals in SLM-processed parts in (a) Fig. 5a; (b) Fig. 5b; (c) Fig. 5c; (d) Fig. 5d.

Unlike the ambiguous epitaxial characteristics shown in Figs. 5a and 6a, the columnar γ dendrites generally exhibited the epitaxial growth with a higher degree of clustering on decreasing the scan speed (Figs. 5b and 6b). As a general rule, most of the heat induced by laser radiation was transmitted through the substrate or previous solidified materials, which in turn facilitated the formation of typical columnar dendrite architectures along the building direction [33]. However, the crystal nucleation and grain growth morphologies were determined by homologous kinetics principles to a great extent [34]. With the considerable decrease of scan speed, the speed of heat dissipation within the molten pool was limited owing to a longer residence of laser beam at a local zone. The comparatively prolonged cooling time therefore provided strengthened kinetics qualifications for the columnar nucleation and growth. A clustering steady state was obtained at the end of the solidification process, due to the relatively equivalent cooling process in each region of the molten pool. On increasing the applied laser power, the temperature within the molten pool increased considerably since more heat generated during the laser irradiation process. As a result, the internal energy and thermodynamic potentials caused by heat accumulation contributed to the strong epitaxial growth of columnar dendrites and, thereby, improved its dispersion performance (Figs. 5c and 6c). At an optimum laser parameter of 330 J/m, the slender consecutive columnar dendrites were formed due to the sufficient nucleation and growth driving force (Figs. 5d and 6d). Based on the above analysis, it was pertinent to consider that the changes of microstructures of SLM-processed Inconel 718 parts were determined by the input laser energy density. The variations of both heat accumulation and temperature development under different laser energy densities were responsible for the microstructure changes.

Table 3 lists the EDX measured chemical compositions at the core of columnar dendrites that were obtained in different process conditions. As revealed from Table 3, the Ni element content increased sharply from 44.87 wt.% to 54.68 wt.% on increasing η from 275 J/m to 330 J/m. Considering the forming laws and conditions of

Table 3
EDX analysis showing chemical compositions at the core of columnar dendrites of SLM-processed Inconel 718 parts under different laser energy densities.

Element (J/m)	Ni	Cr	Fe	Nb	Mo	Al	Ti
η = 275	44.87	16.81	14.24	10.92	4.43	1.26	2.21
η = 300	53.08	16.73	16.94	4.95	2.94	1.23	1.22
η = 330	54.68	14.06	15.43	6.09	2.9	0.9	1.62

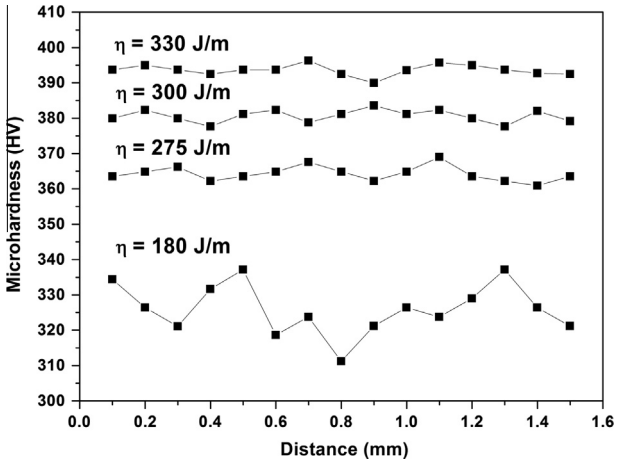

Fig. 7. Microhardness and its distribution of SLM-processed Inconel 718 parts under various processing conditions.

substitution solid solution [35], the surplus incorporation of Ni element resulted in the replacement of other elements composed of γ matrix. According to the XRD data shown in Fig. 2, the base elements contained in γ matrix, sorted by the atomic diameters, are Cr, Fe and Ni. Thus, the incorporation of small sized atomics caused the negative distortion and the resultanted in decrease of lattice spacing, which further improved the deviation of XRD spectra toward higher 2θ values [25].

3.4. Microhardness and wear performance

Fig. 7 shows the microhardness and its distribution measured on the polished sections of SLM-processed parts. On increasing the applied η from 180 J/m to 330 J/m, the average microhardness increased dramatically from 331.9 $HV_{0.2}$ to 395.8 $HV_{0.2}$. The microhardness fluctuation reduced synchronously with the increment of laser energy input, which is believed to be caused by the homogenously dispersed microstructural architectures. It is worth noting that the mean microhardness is almost identical to that ordinarily smelted Inconel 718 parts followed by heat treatment (383 $HV_{0.2}$) as applied η increased to 330 J/m (382.8 $HV_{0.2}$). Obviously, the grain refinement and densification behavior are the main contributions for the enhancement of microhardness. Nevertheless, the effect of intermetallic precipitation phase γ' on microhardness should not be ignored. During the additive manufacturing process, heat was accumulated from the repeated laser radiation on the powder bed. The previous solidified materials experienced an aging treatment with the increment of layers, which motivated the precipitation of γ'. Compared with γ matrix, the γ' phase has not only higher strength but different lattice structure, which generally improved the strength of parts by means of forming lattice misfits and thus coherent stress [36]. In addition to the preceding strengthen factors, the incorporation of Ni element in γ matrix also contributed to the increment of microhardness. The negative

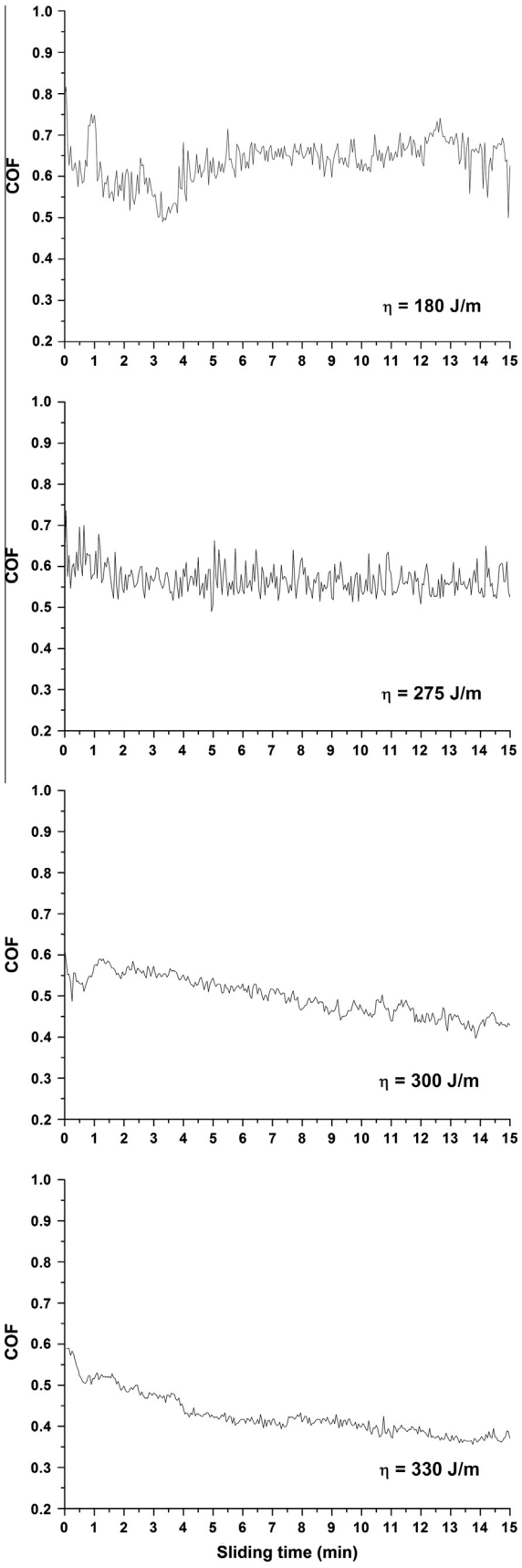

Fig. 8. COFs of SLM-processed Inconel 718 parts using various processing conditions.

distortion induced by the incorporation of Ni atomics restricted the dislocation movement and, thereby, increased the microhardness of SLM-processed parts [37]. In view of the above analysis, the microhardness of the present Inconel 718 parts was enhanced by densification behavior, grain refinement, precipitation strengthening and solid-solution strengthening.

The variations of COFs and wear rates of SLM-processed parts are provided in Figs. 8 and 9, respectively. It was apparent that the applied η exerted a key role in influencing the obtainable wear performance. On increasing η from 180 J/m to 330 J/m, the average COF decreased slightly from 0.62 to 0.58 and the attendant wear rate from 9.12×10^{-4} mm^3/N m to 7.35×10^{-4} mm^3/N m. In addition, the COF values of the corresponding samples both showed an apparent fluctuation behavior with increasing sliding time. The average COF value decreased to 0.49 at a higher η of 300 J/m, leading to the reduced wear rate of 5.66×10^{-4} mm^3/N m. As the applied η increased to 330 J/m, the COF declined gradually until a steady state value of 0.36 was obtained, in which the wear rate reduced to the lowest of 4.64×10^{-4} mm^3/N m.

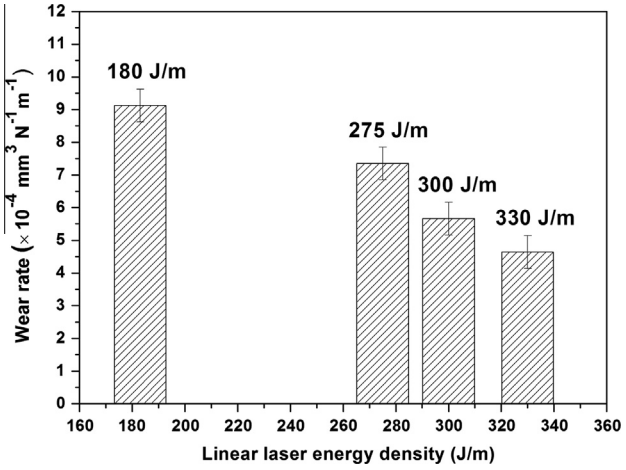

Fig. 9. Wear rates of SLM-processed Inconel 718 parts using different processing parameters.

In order to have a deep understanding of the frictional and wear characteristics of the corresponding parts, the morphologies of worn surfaces are illustrated in Fig. 10. In general, the SLM-processed Inconel 718 specimens exhibited relatively good wear performance without any grooves or cracks after friction. Nevertheless, as shown in Fig. 10, the worn surface morphologies varied greatly from the applied η. At a lower η of 180 J/m, the worn surface was considerably rough with evidence of observed granular wear debris and delamination (Fig. 10a). Such microstructures indicated that the specimen experienced severe adhesive wear, which in turn resulted in a relatively higher wear rate (Fig. 9). The worn surface became much smoother and free of any abrasive fragments as η increased to 275 J/m. In this circumstance, a mild adhesive wear was occurred at the contacts between the specimen and the GCr15 ball, causing the formation of adhesion tribolayer in local zone (Fig. 10b). As η was elevated to 300 J/m, the consecutive adherent tribolayer was observed to be covered on the worn surface (Fig. 10c). When an increased η of 330 J/m was settled properly, a smooth and dense wear track was formed, showing no significant fractures on the worn surface (Fig. 10d).

During the wear tests, the counterface ball slid against the surface continuously, whereas the wear performance was primarily influenced by hardness and related microstructural features of corresponding parts [38]. At a lower laser energy density input, the limited hardness triggered the higher wear rate under the effect of mechanical shear force between the sliding surfaces. The marked fluctuation of COF values were attributed to the formation of coarsened columnar dendrites (Fig. 5a). The wear resistance was enhanced owing to the refined microstructures (Fig. 5b), as well as improved hardness (Fig. 7), on increasing the applied laser energy densities. However, the clustered γ dendrites gave rise to the fluctuations of COF values at this circumstance. The formed protective adherent tribolayer on worn surfaces, as shown in Fig. 10c and d, made considerable contributions to the further improved wear

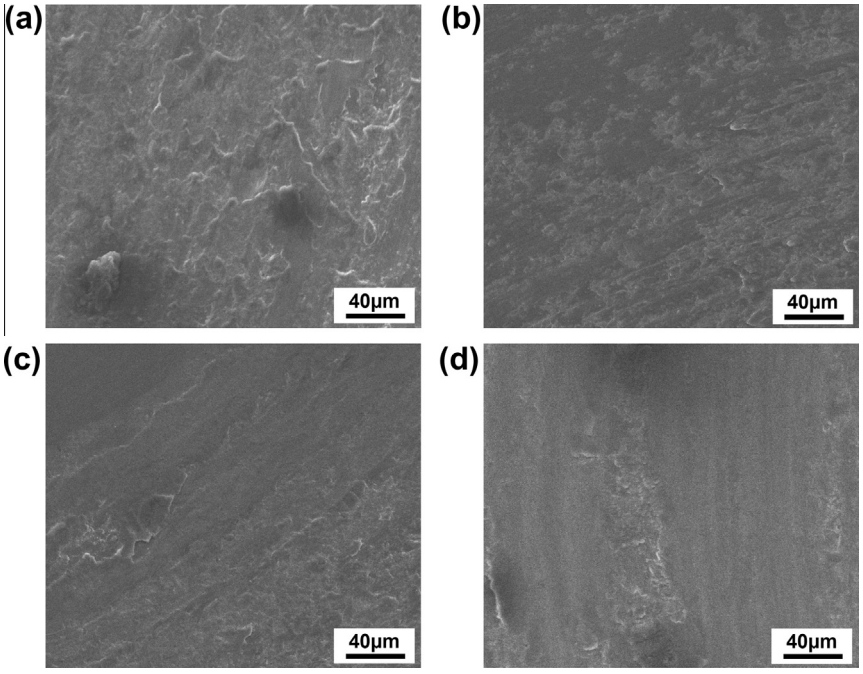

Fig. 10. SEM images showing characteristic morphologies of worn surfaces of SLM-processed Inconel 718 parts at various laser energy densities: (a) 180 J/m; (b) 275 J/m; (c) 300 J/m; (d) 330 J/m.

performance of SLM-processed parts. Thus, it was reasonable to consider that as the input laser energy density increased, the dominant mechanism of material removal during sliding process probably changed from the sliding friction to the rolling friction, which produced the self-lubricating ability [39].

3.5. High-temperature oxidation properties

The oxidation kinetic curves of SLM-processed Inconel 718 parts at 1123 K in still air are summarized in Fig. 11. Generally, the kinetic behavior of the alloy processed at various conditions followed a parabolic law [40]. The mass gains of all specimens increased linearly in the initial stage (until 10 h), whereas varied dramatically in the subsequent oxidation process. As can be seen from Fig. 11, at a lower η of 180 J/m, the weight gain still increased markedly until 70 h though the slope of the curve became gentled. Other specimens, however, showed quite dissimilar tendencies where the oxidation kinetic curves retained almost parallel to the time axis with slight increment. Comparing with the previous results that were focused on the oxidation behavior of Inconel 718 in a cast form [41], the SLM-processed Inconel 718 superalloy fabricated at an optimal 330 J/m in the present study indeed showed good high-temperature oxidation resistance. However, the high-temperature oxidation resistance of the samples prepared using other SLM parameters showed a slight decrease.

In the early process of oxidation, the primary mechanism of oxidation was chemical adsorption while the oxidation rate was controlled by chemical reaction between the sample surface and the ambient atmosphere [42]. In this case, the oxygen inside the furnace chamber directly reacted with the oxide forming elements on the sample surface and, thus, facilitating the linear growth of mass gain with the exposure time elapsing. As the oxidation process proceeded, the sample surface was covered by oxidation film and the dominated oxidation mechanism at present transmitted from chemical adsorption to diffusion [42]. The oxidation scale formed on sample surfaces could act as a diffusion barrier that impeded the oxygen atoms from combining with oxidizable elements consecutively. It was therefore deduced that the slightly increased mass was ascribed to the lower diffusion coefficients within the later oxidation process [43]. However, the kinetic behavior at lower η of 180 J/m did not follow the common rule in the later process of oxidation, which was believed to be caused by peeling off of oxidation film and the subsequent further oxidation of exposed fresh sample surface [44]. Further investigations revealed that the spallation may result from the combined effect of internal stress of oxides scale, which was generated during the cooling process of weighting, and the differential thermal coefficient expansions between the oxides scale and substrate. Essentially, the obtained dense and thin oxidation films could be a function of refined grain size in corresponding parts [45]. According to Wagner's theory [46], the critical concentration of external oxidation of active elements, such as Cr and Al, were greatly reduced by grain refinement. Therefore, the formation of dense Cr_2O_3 film, as a result of selective external oxidation, protected the substrate from further oxidation. In addition, the uniformity of microstructures and relative densities of SLM-processed parts played a significant role in influencing the oxidation process.

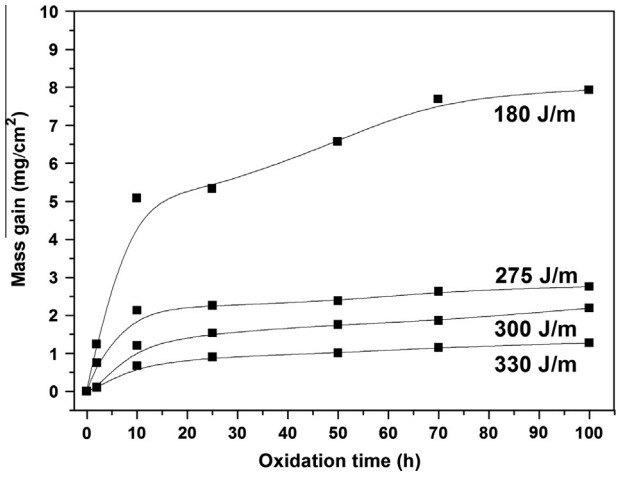

Fig. 11. The oxidation kinetic curves of SLM-processed Inconel 718 parts at different processing parameters.

4. Conclusions

The present article reported on the densification, microstructure and properties of selective laser melting (SLM) processed Inconel 718 parts. The main conclusions were summarized as follows:

(1) The densification response of Inconel 718 parts was controlled by the applied laser energy density. The densification level was restricted at a relatively lower laser energy density, due to the occurrence of open-pores and balling effect. A near-full 98.4% density was achieved as a laser energy density of 330 J/m was properly settled.
(2) The typical microstructures of SLM-processed Inconel 718 parts experienced successive changes: coarsened columnar dendrites – clustered dendrites – slender and uniformly distributed columnar dendrites, on increasing laser energy density.
(3) The optimally prepared Inconel 718 parts had a uniform microhardness distribution with an increased mean value of 395.8$HV_{0.2}$. A considerably low friction coefficient of 0.36 without any apparent fluctuation and a decreased wear rate of 4.64×10^{-4} $mm^3/N\,m$ were obtained in sliding wear tests. The combined influence of elevated microhardness and the formation of adherent tribolayer contributed to the improvement of wear performance.
(4) The optimum high-temperature oxidation resistance of SLM-processed Inconel 718 parts was achieved as applied laser energy density increased to 330 J/m. The refined microstructural architectures were confirmed to be responsible for the enhancement of high-temperature oxidation property with evidence of lower mass gains on the sample surfaces.

Acknowledgments

The authors gratefully appreciate the financial support from the National Natural Science Foundation of China (No. 51104090 and No. 51322509), the Outstanding Youth Foundation of Jiangsu Province of China (No. BK20130035), the NUAA Fundamental Research Funds (No. NE2013103), and the Green Talents Project of the German Federal Ministry of Education and Research (BMBF).

References

[1] M. Ahmad, J.I. Akhter, M. Shahzad, M. Akhtar, J. Alloys Comp. 457 (2008) 131–134.
[2] L. González-Fernández, L. del Campo, R.B. Pérez-Sáez, M.J. Tello, J. Alloys Comp. 513 (2012) 101–106.
[3] G. Cam, M. Kocak, Int. Mater. Rev. 43 (1998) 1–44.
[4] F.C. Liu, X. Lin, C.P. Huang, M.H. Song, G.L. Yang, J. Chen, W.D. Huang, J. Alloys Comp. 509 (2011) 4505–4509.
[5] S.H. Chang, J. Alloys Comp. 486 (2009) 716–721.

[6] L. Zheng, G. Schmitz, Y. Meng, R. Chellali, R. Schlesiger, Crit. Rev. Solid State Mater. Sci. 37 (2012) 181–214.
[7] C.M. Kuo, Y.T. Yang, H.Y. Bor, C.N. Wei, C.C. Tai, Mater. Sci. Eng. A 510 (2009) 289–294.
[8] Q.L. Zhang, J.H. Yao, J. Mazumder, J. Iron Steel Res. Int. 18 (2011) 73–78.
[9] B. Izquierdo, S. Plaza, J.A. Sanchez, I. Pombo, N. Ortega, Appl. Surf. Sci. 259 (2012) 780–790.
[10] L. Zheng, M.C. Zhang, J.X. Dong, Mater. Des. 32 (2011) 1981–1986.
[11] Z.M. Wang, K. Guan, M. Gao, X.Y. Li, X.F. Chen, X.Y. Zeng, J. Alloys Comp. 513 (2012) 518–523.
[12] S. Dadbakhsh, L. Hao, J. Alloys Comp. 541 (2012) 328–334.
[13] B. Song, S.J. Dong, P. Coddet, G.S. Zhou, S. Ouyang, H.L. Liao, C. Coddet, J. Alloys Comp. 579 (2013) 415–421.
[14] B. Vrancken, L. Thijs, J.P. Kruth, J. Van Humbeeck, J. Alloys Comp. 541 (2012) 177–185.
[15] B.C. Zhang, N.E. Fenineche, H.L. Liao, C. Coddet, J. Mater. Sci. Technol. 29 (2013) 757–760.
[16] B.C. Zhang, H.L. Liao, C. Coddet, Appl. Surf. Sci. 279 (2013) 310–316.
[17] L.X. Dong, H.M. Wang, J. Alloys Comp. 465 (2008) 83–89.
[18] B.C. Zhang, H.L. Liao, C. Coddet, Vacuum 95 (2013) 25–29.
[19] I. Yadroitsev, I. Smurov, Phys. Procedia 5 (2010) 551–560.
[20] S.H. Fu, J.X. Dong, M.C. Zhang, X.S. Xie, Mater. Sci. Eng. A 499 (2009) 215–220.
[21] P.L. Blackwell, J. Mater. Process. Technol. 170 (2005) 240–246.
[22] X.M. Zhao, J. Chen, X. Lin, W.D. Huang, Mater. Sci. Eng. A 478 (2008) 119–124.
[23] D.D. Gu, Y.F. Shen, J. Alloys Comp. 473 (2009) 107–115.
[24] K.N. Amato, S.M. Gaytan, L.E. Murr, E. Martinez, P.W. Shindo, J. Hernandez, S. Collins, F. Medina, Acta Mater. 60 (2012) 2229–2239.
[25] Y. Zhou, G.H. Wu, Analysis Methods in Materials Science—X-ray Diffraction and Electron Microscopy in Materials Science, second ed., Harbin Institute of Technology Press, Harbin, 2007.
[26] I. Takamichi, I.L.G. Roderick, The Physical Properties of Liquid Metals, Clarendon Press, Oxford, 1993.
[27] H.J. Niu, I.T.H. Chang, Scripta Mater. 39 (1998) 67–72.
[28] A. Simchi, H. Pohl, Mater. Sci. Eng. A 359 (2003) 119–128.
[29] D.D. Gu, Y.F. Shen, Mater. Des. 30 (2009) 2903–2910.
[30] Q.Y. Pan, X. Lin, W.D. Huang, Y.M. Li, Y.H. Zhou, Prog. Nat. Sci. 8 (1998) 79–86.
[31] D.D. Gu, Y.C. Hagedorn, W. Meiners, K. Wissenbach, R. Poprawe, Surf. Coat Technol. 205 (2011) 3285–3292.
[32] F.C. Liu, X. Lin, G.L. Yang, M.H. Song, J. Chen, W.D. Huang, Opt. Laser Technol. 43 (2011) 208–213.
[33] G.P. Dinda, A.K. Dasgupta, J. Mazumder, Mater. Sci. Eng. A 509 (2009) 98–104.
[34] V. Erukhimovitch, J. Baram, Phys. Rev. B 50 (1994) 5854–5856.
[35] W.B. Pearson, L.T. Thompson, Can. J. Phys. 35 (1957) 349–357.
[36] A. Strondl, R. Fischer, G. Frommeyer, A. Schneider, Mater. Sci. Eng. A 480 (2008) 138–147.
[37] T.J. Rupert, J.C. Trenkle, C.A. Schuh, Acta Mater. 59 (2011) 1619–1631.
[38] L.Y. Sheng, F. Yang, T.F. Xi, J.T. Guo, J. Alloys Comp. 554 (2013) 182–188.
[39] M.Y. Niu, Q.L. Bi, S.Y. Zhu, J. Yang, W.M. Liu, J. Alloys Comp. 555 (2013) 367–374.
[40] N. Hussain, K.A. Shahid, I.H. Khan, S. Rahman, Oxid. Met. 43 (1995) 363–378.
[41] G.A. Greene, C.C. Finfrock, Oxid. Met. 55 (2001) 505–521.
[42] D.S. Li, Q.X. Dai, X.N. Cheng, R.R. Wang, Y. Huang, J. Iron Steel Res. Int. 19 (2012) 74–78.
[43] R. Haugsrud, Corros. Sci. 45 (2003) 211–235.
[44] L. Zheng, M.C. Zhang, R. Chellali, J.X. Dong, Appl. Surf. Sci. 257 (2011) 9762–9767.
[45] R. Haugsrud, Mater. Sci. Eng. A 298 (2001) 216–226.
[46] C. Wagner, J. Electrochem. Soc. 99 (1952) 369–380.